



Fabrication of B doped g-C₃N₄/TiO₂ heterojunction for efficient photoelectrochemical water oxidation

Weiqian Kong^a, Xiaofan Zhang^{a,*}, Binbin Chang^a, Yannan Zhou^a, Shouren Zhang^a, Guangli He^a, Baocheng Yang^a, Junjie Li^b

^a Henan Provincial Key Laboratory of Nanocomposite and Applications, Institute of Nanostructured Functional Materials, Huanghe Science and Technology College, Zhengzhou, Henan, 450006, China

^b Research Technologies, Indiana University, 535 West Michigan Street, Indianapolis 46202, USA

ARTICLE INFO

Article history:

Received 26 April 2018

Accepted 12 June 2018

Available online 14 June 2018

Keywords:

Hetero-junction

B doped g-C₃N₄

TiO₂ nanorods

Photoelectrochemical

Water oxidation

ABSTRACT

With the development of clean and renewable energy, hydrogen produced via photoelectrochemical (PEC) water splitting has attracted considerable attention. However, to develop the photoanodes with stable and excellent PEC ability is still a big challenge. In our work, TiO₂ nanorods decorated with boron doped g-C₃N₄ (BCN/TiO₂) is fabricated via thermal polymerization method to improve the PEC performance. The BCN/TiO₂ displays 4-fold increase of the photocurrent density (1.01 mA cm⁻²) at 1.23 V vs. RHE under irradiation (100 mW cm⁻², AM 1.5 G). And the onset potential of BCN/TiO₂ exhibits a negative shift with 100 mV. Attributed to the broad light absorption of BCN and hetero-junction forming between BCN and TiO₂, the IPCE value is increased to 87.8% in 380 nm, and the charge separation and transfer efficiency are both increased. Doping metal-free inorganic material with heteroatoms is a simple and efficient strategy to increase the light absorption within visible light and charge transfer efficiency in PEC and photocatalytic applications.

© 2018 Elsevier Ltd. All rights reserved.

1. Introduction

Photoelectrochemical (PEC) water splitting is a promising strategy to obtain hydrogen which is the cleanest energy because of its recyclability, environmental friendliness and high energy conversion efficiency [1–4]. The solar-to-hydrogen (STH) efficiency is related to the light absorption, the separation of photo-generated charge carries and kinetics of surface reaction [5]. TiO₂ is one of the most attractive semiconductors as photoanode due to the low toxic and eco-friendly nature in addition to its low cost [3,6]. However, TiO₂ can only absorb UV light ($E_g = 3-3.2$ eV) and possess rapid electron/hole recombination and slow water oxidation kinetics [7,8]. The STH efficiency of the TiO₂ is still very low. Until now, numerous methods have been developed to solve these problems. The various nanostructure TiO₂ have been investigated [9,10], out of which the 1D TiO₂ nanorods (NRs) has attracted more attention as it exhibits more activate sites and provides a direct electron transport pathway for electrons [11]. Doping with non-

metallic element (C [12], N/Si [13], B [14]), noble-metal decoration [15] are studied to narrow the band gap of TiO₂. Beyond that, establishing heterojunction (TiO₂/WO₃ [16], TiO₂/In₂O₃ [17], NiTiO₃/TiO₂ [18]), or coupling with co-catalysts [19] are also investigated to improve the photoresponse of TiO₂ in visible region and improve the separation of photogenerated electrons.

Graphitic carbon nitride (g-C₃N₄) as a metal-free inorganic semiconductor is a promising material in PEC application, which possesses high thermal and chemical stability, relatively low band gap energy (E_g) of 2.7 eV, high valence band (1.8 eV) and conduction band positions (−0.9 eV) [20,21]. Based on the proper band gap between TiO₂ and g-C₃N₄, g-C₃N₄/TiO₂ heterojunction has attracted more attention in photocatalytic, photoelectrochemical and degradation applications [22–25]. However, the performance of g-C₃N₄/TiO₂ is still limited by the small specific surface area, grain boundary effects and the poor electrical conductivity of g-C₃N₄ [26,27]. Recently, doping g-C₃N₄ with heteroatoms has been widely used in photoelectrochemical cell due to its excellent light absorption and improved electric properties [28,29]. For example, sulfur and iodine doped g-C₃N₄ can narrow the bandgap, and even decrease the reaction over-potential in comparison to g-C₃N₄ as demonstrated by DFT calculations [30,31]. Yan et al. fabricated B

* Corresponding author.

E-mail address: xiaofanzhang@infm.hhstu.edu.cn (X. Zhang).

doped g-C₃N₄ via heating the mixture of melamine and boron oxide to photo-degrade rhodamine B and methyl orange [32]. The results demonstrated B doped g-C₃N₄ exhibited more excellent activity than that of g-C₃N₄ attributed to the extended light absorption and the defected structure induced by boron doping. Ruan et al. fabricated a nanojunction architecture photoanode composing B doped g-C₃N₄ nanolayer and bulk g-C₃N₄. This nanojunction overcame some limitation of g-C₃N₄ and improved the charge transfer and charge separation efficiency [33]. These reports demonstrate that B doped g-C₃N₄ exhibits great potential in enhancing PEC application via forming hetero-junction. However, B doped g-C₃N₄ decorated TiO₂ nanorods has not been investigated for PEC water oxidation.

As discussed above, we construct a hetero-junction consisting of the TiO₂ nanorods (NRs) and B doped g-C₃N₄ (BCN) via in-situ thermal polymerization method. The introduction of B doping into g-C₃N₄ can extend the light absorption and improve the conductivity. The formed heterojunction between TiO₂ and BCN is further expected to improve the light absorption, promote the charges separation and transfer process. Therefore, the BCN/TiO₂ photoanode exhibits four times higher photocurrent density (1.01 mA cm⁻² at 1.23 V vs. RHE) than that of the TiO₂, following with a 100 mV cathodically shifted onset potential in 1 M NaOH (pH = 13.6) solution. Furthermore, the charge separation increases and the transfer efficiency increase 1.4 and 2.5 times (1.23 V vs. RHE) than that of TiO₂ photoanode. The BCN/TiO₂ shows a constant evolution H₂ with 16.1 μmol h⁻¹ cm⁻² at 1.23 V vs. RHE.

2. Experimental

2.1. Prepared of all electrodes for electrochemical water oxidation

The TiO₂ nanorods (TiO₂ NRs) were grown onto FTO substrate by a hydrothermal method according to our previous report [12]. In a typical experiment, the concentrated hydrochloric acid (HCl), deionized (DI) water and titanium isopropoxide (TTIP, Sigma-Aldrich, 97%) was prepared a homogeneous solution according to the volume ratio of 3:3:0.1. Then the precursor solution was transferred into a Teflon-lined autoclave reactor, in which a piece of FTO was placed with the conductive side facing down. The hydrothermal reaction was conducted at 150 °C for 12 h in an oven and cooled down to room temperature naturally. The obtained film was washed with DI water and dried at 60 °C. Finally, the sample was annealed at 450 °C for 2 h and the rutile TiO₂ were obtained.

Then the BCN/TiO₂ and the contrast photoanode of g-C₃N₄ modified TiO₂ (CN/TiO₂) were prepared via in-situ immersing and annealing approach. In a typical experiment, 1 g urea with 0.7 mL 0.1 M boracic acid and no boracic acid were separately added into 14 mL H₂O solvent to obtain a homogeneous solution. Then the prepared TiO₂ was immersed into the mixed solution and maintained for 30 min. Then taken them out and dried at 80 °C. Next, the samples were heated to 550 °C with a heating rate of 5 °C/min, and kept for 3 h in tube furnace. Then the BCN/TiO₂ and CN/TiO₂ photoanodes can be obtained, respectively. Besides, the pure bulk BCN powder was also prepared for comparison. In order to maintain the B doping content in BCN consistent with BCN/TiO₂, 1 g urea and 0.7 mL of 0.1 M boracic acid were added into a crucible with a cover, then heated to 550 °C with a heating rate of 5 °C/min in tube furnace and maintained at this temperature for 3 h in the Ar atmosphere. After cooling down to room temperature, the pale yellow BCN powder was obtained.

2.2. Materials and characterization

All the chemicals were used as received, and the solutions were

made with Milli-Q water. The morphology was characterized with scanning electron microscope (SEM, FEI Quanta 250 FEG) and transmission electron microscopy (TEM, FEI/Philips Tecnai G2 20) with an accelerating voltage of 200 kV. The X-ray photoelectron spectroscopy (XPS) data was obtained on a Thermo Scientific K-Alpha X-ray photoelectron spectrometer with a monochromatized Mg Kα X ray source (hν = 1283.3 eV). The binding energy shifts were corrected by using the C1s level at 284.8 eV as an internal standard to compensate for the surface-charging effect during data analysis. X-ray diffraction (XRD) patterns were monitored by a Bruker D8 diffractometer using Cu Kα radiation (λ = 0.15418 nm) as an X-ray source. UV–vis spectra were recorded by U-4100 (HITA-CHI) spectrophotometer. The photoluminescence (PL) spectra were recorded at room temperature with F-4600 (HITACHI) luminescence spectrometer. Fourier transform infrared (FT-IR) spectra was collected on a FT-IR spectrometer (Nicolet iS5, Thermo Scientific) using a standard KBr pellet technique.

2.3. Photoelectrochemical measurements

The PEC performance data were obtained with the CHI 760E (Shanghai Chenhua, China) workstation with 1 M NaOH (pH = 13.6) solution as the supporting electrolyte. In addition, a three-electrode system was used in our experiment. The prepared photoanodes were used as working electrodes, the platinum (Pt) sheet was used as counter electrode and the saturated calomel electrode (SCE) was used as reference electrode. The electrolyte was purged with high-purity Ar for 30 min to remove dissolved oxygen and carbon dioxide, which can prevent the compete reaction from oxygen reduction and the decreasing of the pH value [34]. The solution is irradiated using a 500 W Xe-lamp (CEL-500, CEAULIGHT), which is coupled with an AM 1.5 G filter. The light power density was calibrated to 100 mW cm⁻² with light power meter (CEL-NP2000-2). Linear sweep voltammetry (LSV) was performed with a scan rate of 10 mV s⁻¹. The stability test was carried out with amperometric measurements (i-t) under illumination (100 mW cm⁻², AM 1.5 G), which the voltage was at a fixed potential of 1.23 V vs. RHE. The monochromatic IPCE was also calculated at a fixed potential of 1.23 V vs. RHE using different cut-off filters (365 nm, 380 nm, 420 nm, 435 nm, 450 nm, 475 nm, 500 nm and 550 nm). The electrochemical impedance spectroscopy (EIS) was documented in the frequency range of 100 kHz to 0.01 Hz with an AC voltage amplitude of 10 mV at a bias of 0.2 V vs. RHE in 1 M NaOH solution. The Mott-Schottky plot was collected in a potential range of -0.8–0.6 V vs. RHE with a frequency of 1 kHz in the dark. The evolved H₂ and O₂ were detected using gas chromatography (GC-7920, China, detection limit: H₂ 50 ppm, O₂ 1000 ppm) with Ar as a carrier gas. The gas evolution by photoelectrodes was regularly collected by a manual injector quantitatively analyzed by gas chromatography (GC). And the amount gases were calculated according to the corresponding standard curve, respectively. All the electrochemical experiments were carried out at room temperature. All the potential in the experiment was converted to reversible hydrogen electrode (RHE) by the Nernst equation:

$$E_{\text{RHE}} = E_{\text{vs.SCE}} + E_{\text{SCE}}^{\circ} + 0.059\text{pH}$$

where the E_{SCE}° is 0.2412 V at 25 °C.

3. Results and discussion

As illustrated in Fig. 1, the TiO₂ NRs photoanodes is obtained via hydrothermal method [12] was chosen as a prototype for investigating the PEC performance. Then the TiO₂ NRs is decorated with BCN after impregnation and annealing treatment.

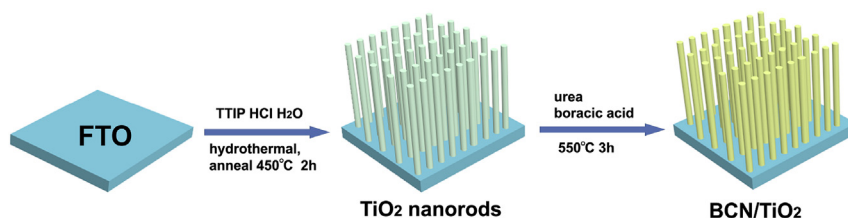


Fig. 1. Schematic diagram of the BCN/TiO₂ photoanode.

SEM and TEM images are characterized the morphologies and structures of the TiO₂ and BCN/TiO₂. As shown in Fig. 2a, the TiO₂ are uniformly grown onto FTO with the average diameter of 80–150 nm and a length of 3 μ m (inset of Fig. 2a). The BCN islands are clearly observed on TiO₂ via a thermal polymerization route (Fig. 2b). Fig. 2c provides the clear morphology of a single nanorod of TiO₂. The lattice fringe of 0.323 nm (inset of Fig. 2c) is corresponding to the (110) plane of tetragonal TiO₂. Fig. 2d shows the TiO₂ is all surrounded with the BCN film, which agrees well with the linear EDX image (Fig. S1). The boundary between BCN and TiO₂ can be distinctly observed in Fig. S2. The thickness of the surrounded BCN film is calculated to be 2–10 nm. To further testify the existence of BCN, the FT-IR spectra of the TiO₂, BCN, and BCN/TiO₂ are further confirmed (Fig. S3). Compared to the TiO₂ NRs and BCN, the typical peaks of BCN can be clearly observed in BCN/TiO₂ at $\sim 3200\text{ cm}^{-1}$ (C–H) and $1250\text{--}1650\text{ cm}^{-1}$ (C–N) [35]. And the characteristic peak of Ti–O is found at $500\text{--}1000\text{ cm}^{-1}$ [36]. These results indicate the existence of BCN in the BCN/TiO₂.

The X-ray photoelectron spectroscopy (XPS) is analyzed to determine the element analysis and chemical composition of all samples. Fig. 3 illustrates the XPS survey spectra and high-resolution XPS spectra of different elements. Fig. 3a represents the presence of B, C, O, N and Ti atoms, which is consistent with the

linear EDX image. Fig. 3b has displayed the high-resolution B 1s peaks of BCN and BCN/TiO₂. The peak at 192.0 eV of the BNC is corresponding to the typical B–N bond [37,38]. The peak at 190.7 eV of the BCN/TiO₂ is at a lower binding energy than that of BCN, indicating some of the boron atoms are less electropositive than that of BCN [37]. The characteristic peak of Ti–O–B–O–Ti (191.6 eV) is not discovered in BCN/TiO₂ [14], indicating no B atom doped into the TiO₂ nanorod lattice for BCN/TiO₂. Fig. 3c has shown the high-resolution spectra of Ti 2p in BCN and BCN/TiO₂. The Ti 2p XPS spectrum is divided by Ti 2p_{3/2} and Ti 2p_{1/2} peaks. For pristine TiO₂, the Ti can be fitted with the binding energies of 458.8 eV and 464.6 eV peak for Ti 2p_{3/2} and Ti 2p_{1/2}, respectively [39,40]. After modified with BCN, the two Ti 2p peaks decrease to 458.6 eV and 464.4 eV, respectively. The negative shift of Ti 2p can be attributed to the changing of electron cloud density around TiO₂ surface binding interaction, which is consistent with the positive shift of B atom in BCN/TiO₂. This phenomenon predicts an electron transfer from BCN to TiO₂ [19]. As shown in Fig. 3d, the C1s XPS spectrum of BCN/TiO₂ reveals three different signals at 284.7, 286.0 and 288.7 eV, respectively. The peak at 284.8 eV is ascribed to graphitic carbon. The weaker C peak located at 288.7 eV can be assigned to sp²-bonded carbon (N–C=N) [20]. As a result, the BCN is successfully covered onto the surface of TiO₂ photoanode, which is

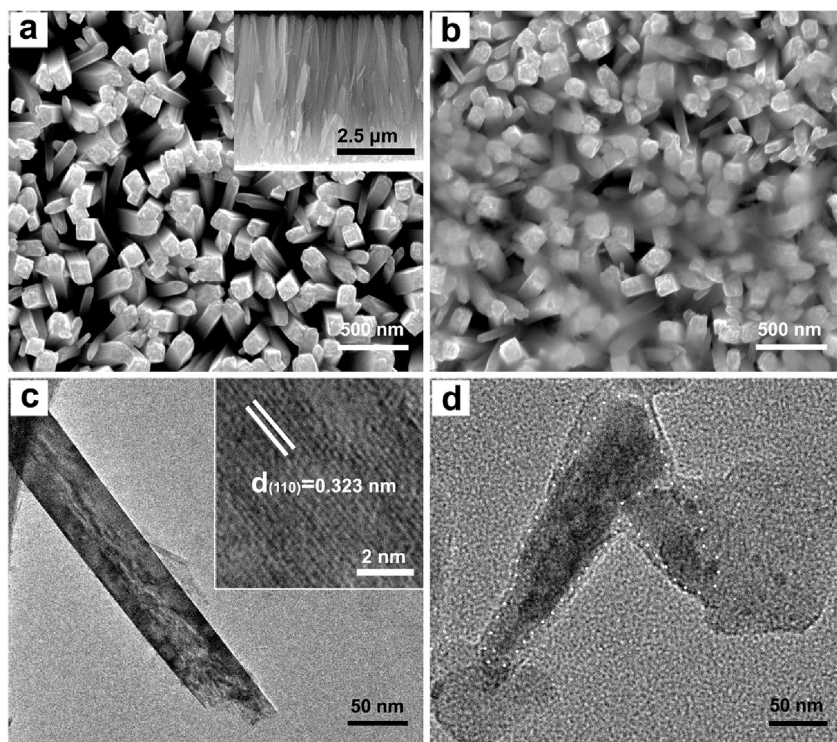


Fig. 2. SEM images of the TiO₂ (a) and BCN/TiO₂ (b). TEM images of the TiO₂ (c) and BCN/TiO₂ (d).

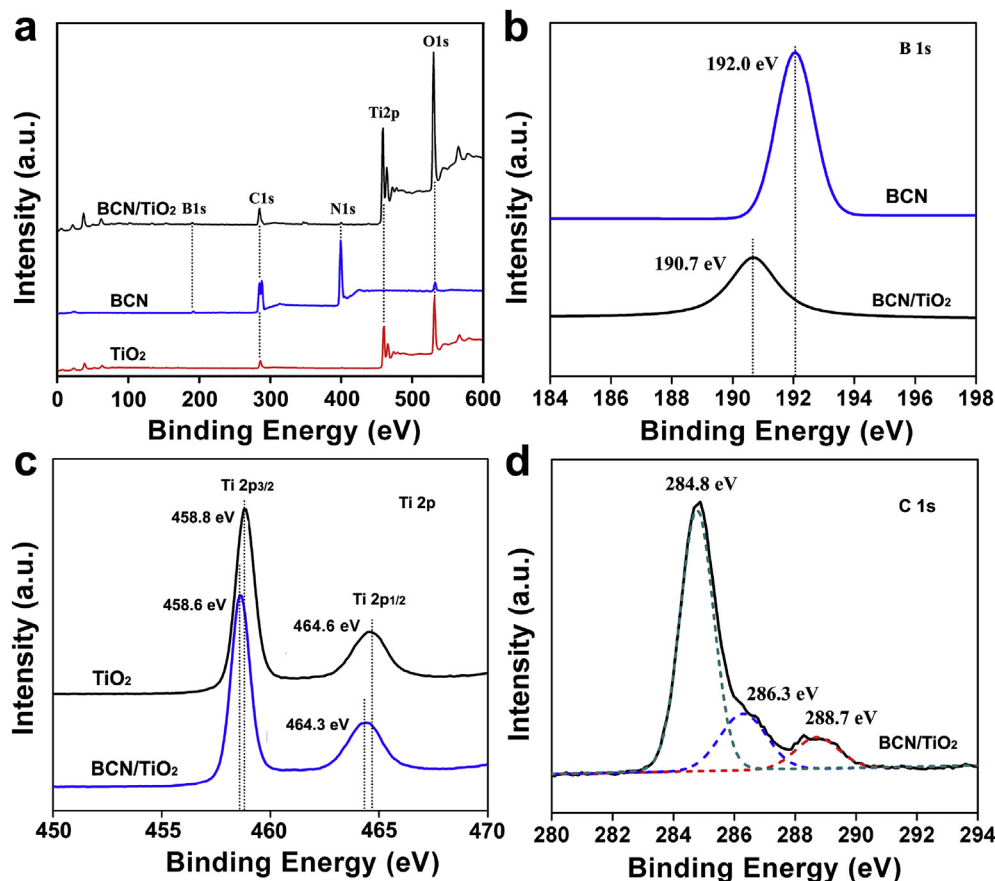


Fig. 3. (a) The full XPS spectra of the TiO₂, BCN and BCN/TiO₂. The high-resolution XPS spectra of B 1s (b), Ti 2p (c) and C 1s (d).

consistent with the results of the TEM images and FT-IR spectra.

The crystal structure is revealed by X-ray diffraction (XRD) as shown in Fig. 4a. The obvious peak of BCN spectrum at 27.5° can be indexed to the (002) interlayer spacing and correspond to the characteristic inter-planar staking peak of aromatic system [31]. The diffraction peaks at 36.4°, 62.5° and 65.8° are corresponding to the (101), (002) and (112) crystal plans of rutile TiO₂, respectively (JCPDS 21-1276) [41]. The BCN/TiO₂ shows no diffraction peaks at 27.5°, owing to a small amount of BCN. Apart from the peaks of the BCN and TiO₂, there is no additional peak can be observed in BCN/TiO₂, indicating the BCN can not change the crystal phase of TiO₂. In order to investigate the influence of BCN on the light absorption,

the normalized UV–vis spectra of TiO₂, BCN and BCN/TiO₂ are collected. As Fig. 4b shown, the spectrum of TiO₂ shows a strong absorption in UV region but decreases sharply at the wavelength of 410 nm. The slight absorption in visible region is caused by the undetected light scattering, which nearly has no effect during the PEC water splitting process [42]. The absorption edge of BCN is about 470 nm. It can be clearly observed that the BCN/TiO₂ show slightly red-shifted compared to TiO₂, which is ascribed to the light absorption of BCN [43]. According to the Tauc plot ($(\alpha h\nu)^{1/2}$ vs. $h\nu$), the band gap of TiO₂ and BCN are calculated to be 3.0 eV and 2.69 eV, respectively [12,44]. The changing of band gap can be attributed to the bonding between BCN and TiO₂. The result

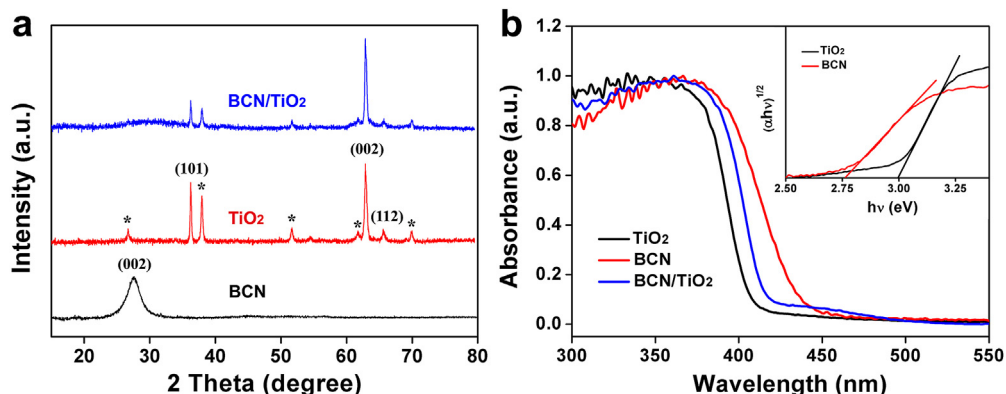


Fig. 4. XRD patterns (a) and the normalized UV–vis spectra (b) of the TiO₂, BCN and BCN/TiO₂ (Inset of Fig. 2b is the corresponding Tauc plots).

indicates an extended absorption is endowed to the BCN/TiO₂ which implies a better PEC performance. PL spectra is a convenient technology to indirectly evaluate the charge separation and transfer abilities [45,46]. As Fig. S4 shown, the PL intensity of CN/TiO₂ is smaller than that of the TiO₂. For BCN/TiO₂, the PL intensity can be further decreased, implying the charge separation may be further promoted by BCN/TiO₂ than that of CN/TiO₂. These results demonstrate the increased light absorption and improved separation of photo-generated charge carriers will be beneficial for PEC water oxidation.

The PEC performance of all prepared photoanodes are investigated both in dark and light illumination and the results are shown in Fig. 5. The LSV curves of the TiO₂ and BCN/TiO₂ were recorded in 1 M NaOH electrolyte under light irradiation (AM 1.5 G, 100 mW cm⁻²). Firstly, a series of BCN/TiO₂ obtained with different concentrations of BCN were tested to optimize the content of BCN. The prepared BCN/TiO₂ was denoted as x % BCN/TiO₂ according to the content of the urea precursor (x wt%), and the results are shown in Fig. S5. Among them, the highest photocurrent density can be obtained for the BCN/TiO₂ (7%). In the dark, the TiO₂ and BCN/TiO₂ photoanodes show negligible current over the whole potential window (Fig. 5a). For comparison, the photocurrent densities of TiO₂, CN/TiO₂ and BCN/TiO₂ are both measured under light illumination. As shown in Fig. 5a, the photocurrent density of the CN/TiO₂ is 2.9 times higher than that of the pristine TiO₂ (0.23 mA cm⁻², E_{RHE} = 1.23 V). After B doping, the photocurrent density of the BCN/TiO₂ further increases to 1.01 mA cm⁻² (E_{RHE} = 1.23 V), which is approximate four times larger than that of TiO₂. In addition, the onset potential of the BCN/TiO₂ cathodically shifts 100 mV. The incident photo-to-current efficiency (IPCE) is measured under light illumination at 1.23 V vs. RHE with different cut-off filters, which can be calculated with the following equation:

$$\text{IPCE}(\%) = \left[1240 \times J_p / (\lambda \times P(\lambda)) \right] \times 100\%$$

where J_p is the photocurrent density (mA cm⁻²), $P(\lambda)$ is the incident-light power density for each wavelength (mW cm⁻²), and the λ is the incident-light wavelength (nm). As shown in Fig. 5b, the maximum IPCE values of TiO₂ and BCN/TiO₂ are both recorded at 380 nm, which are 36.6% and 87.8%, respectively. Furthermore, in the entire visible region investigated, the IPCE values of BCN/TiO₂ are already two times higher than that of the TiO₂ photoanode (inset of Fig. 5b). In a word, the BCN/TiO₂ shows a better IPCE response over the entire wavelength range investigated, which is well matched with the UV–vis spectra.

To investigate the charge transfer process, the EIS measurement was performed in dark and light illumination (AM 1.5 G, 100 mW cm⁻²) at an AC frequency from 100 kHz to 0.01 Hz. As shown in Fig. 5c, the Nyquist plot of BCN/TiO₂ obtained in dark exhibits a smaller diameter than that of the CN/TiO₂, indicating the conductivity can be improved after B doped g-C₃N₄. Under illumination, the BCN/TiO₂ displays the smallest charge transfer resistance (R_{ct}) among the TiO₂, CN/TiO₂ and BCN/TiO₂ photoanodes, indicating the charge transfer process can be promoted at the interfacial of photoanode/electrolyte. The result indicates the charge-transfer barrier at the electrode interface is decreased, so that the water oxidation reaction is easier to occur and a cathodically shift of onset potential appears [47]. These results agree well with the LSV curves (Fig. 5a) and PL spectra (Fig. S4). In order to deeply investigate the intrinsic electronic properties, Mott-Schottky (MS) plots are collected in dark to obtain the flat-band potential (E_{fb}). Just as Fig. 5d and Fig. S6 shown, the positive slopes of TiO₂ and BCN plots indicate the n-type semiconductor of TiO₂ and BCN. And the flat-band potential (E_{fb}) of TiO₂, CN/TiO₂ and

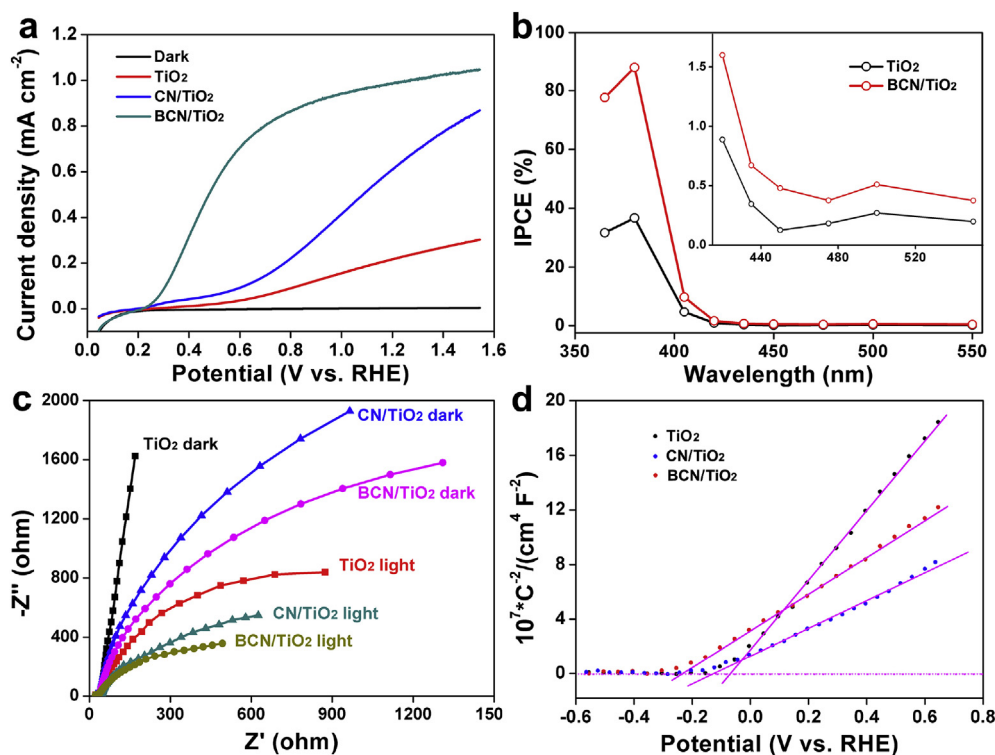


Fig. 5. (a) LSV curves of TiO₂ and BCN/TiO₂ with a scan rate of 10 mV s⁻¹ under light illumination (100 mW cm⁻², AM 1.5 G). (b) IPCE plots of TiO₂ and BCN/TiO₂ obtained at 1.23 V vs. RHE. The inset image is the magnification IPCE data within 400–550 nm. (c) Nyquist plots of the TiO₂, CN/TiO₂ and BCN/TiO₂ measured in dark and under illumination. (d) The Mott-Schottky plots of the TiO₂, CN/TiO₂ and BCN/TiO₂ collected at a frequency of 1 kHz in dark.

BCN/TiO₂ is calculated to be -0.06 V, -0.12 V and -0.23 V vs. RHE, respectively. The negative shift of E_{fb} implies the charge flow from BCN to TiO₂, which decreases the chance of electron/hole recombination [24]. Simultaneously, the MS result demonstrates the BCN/TiO₂ has the highest charge transfer efficiency compared with TiO₂ and CN/TiO₂, which is conducive to improve PEC water oxidation performance.

For further investigating the PEC performance of BCN/TiO₂, the light harvesting efficiency (LHE, $LHE = 1 - 10^{-A}$), charge separation efficiency (η_{sep}) and surface charge transfer efficiency ($\eta_{transfer}$) are calculated. Fig. 6a shows the LHE spectra of the TiO₂ and BCN/TiO₂. It is obvious that the LHE enhancement of the BCN/TiO₂ (1.1 times) is much smaller than the IPCE enhancement (2.4 times), which indicates the extended light absorption is not the main reason for the enhanced PEC performance. In order to explore the detail information of charge separation efficiency and surface charge transfer efficiency, a hole scavenger (Na₂SO₃) was added into the electrolyte during the experiment, which can eliminate the energy loss in the oxidation process [48]. Fig. S7 displays the LSV curves of TiO₂ and BCN/TiO₂ before and after adding 0.1 M Na₂SO₃. Since the hole capture kinetics of Na₂SO₃ at the semiconductor/electrolyte surface is very fast, the charge injection efficiency can be assumed 100% [49]. The photocurrent density of PEC water oxidation can be described by $J_{H_2O} = J_{abs} \times \eta_{sep} \times \eta_{transfer}$ without 0.1 M Na₂SO₃. Thus, the photocurrent density after adding Na₂SO₃ can be calculated by $J_{H_2O} = J_{abs} \times \eta_{sep}$. According to our previous report [50], the J_{abs} of the TiO₂ and BCN/TiO₂ photoanodes are calculated to be 1.6 mA cm^{-2} and 2.0 mA cm^{-2} (Fig. 6b), respectively. The addition of Na₂SO₃ has no effect in changing the pH, light absorption or E_{fb} for the electrodes, so the J_{abs} should be same for each photoanodes. Thus, the η_{sep} and $\eta_{transfer}$ can be obtained by $J_{Na_2SO_3}/J_{abs}$ and $J_{H_2O}/J_{Na_2SO_3}$, respectively. Fig. 6c expresses that the charge separation efficiency of the BCN/TiO₂ is higher (54.9%, vs. 1.23 V) than that of pristine TiO₂ (38.9%, vs. 1.23 V). This implies the recombination of

photo-generated electron/hole pairs is effectively restrained after modified with BCN, owing to the efficient improved charge transfer from BCN to TiO₂. As exhibited in Fig. 6d, the prominent enhanced charge transfer efficiency is observed in BCN/TiO₂ photoanode (91%, vs. 1.23 V), which increases 1.53 times than that of TiO₂ photoanode (36%, vs. 1.23 V). Therefore, the BCN/TiO₂ composite photoanode has excellent photocatalytic activity on PEC water splitting.

The stable performance of the TiO₂ and BCN/TiO₂ electrodes for water oxidation is also investigated. The stabilities are evaluated with amperometric measurements (i-t) under illumination (100 mW cm^{-2} , AM 1.5 G), which the potential is set at 1.23 V (vs. RHE). Fig. 7a has displayed the corresponding i-t curves of BCN/TiO₂ and TiO₂ photoanodes. For BCN/TiO₂ photoanode, the photocurrent density goes steadily with the time increasing and has no obvious decay even after 6 h. On the contrary, the TiO₂ electrode exhibits reduced stability, which the photocurrent density decreases approximately 19% after 6 h. This result indicates that BCN could be contributed to the augmented stability of TiO₂ electrode.

In order to validate whether the anodic photocurrent generated by the photoanode is the exclusive result of O₂ evolution, the produced H₂ and O₂ are both quantified by GC under light irradiation (AM 1.5 G, 100 mW cm^{-2}). In addition, the gas products are injected into gas chromatography (GC) for quantitative analysis. As Fig. 7b shown, the constant H₂ evolution of BCN/TiO₂ photoanode is $\sim 16.1 \mu\text{mol h}^{-1} \text{ cm}^{-2}$ with the testing period of 6 h, which is 10.7 times larger than that of pristine TiO₂ photoanode ($1.5 \mu\text{mol h}^{-1} \text{ cm}^{-2}$). The O₂ evolution of BCN/TiO₂ is about $7.4 \mu\text{mol h}^{-1} \text{ cm}^{-2}$. In addition, the molar ratio of the produced H₂ and O₂ is 2.17, which is close to the theoretical value for overall water splitting. As a consequence, the introduction of BCN indeed enhances the PEC water splitting process.

The mechanism of the BCN/TiO₂ photoanode for enhanced PEC performance is also been proposed (Fig. 8). The valence band (VB)

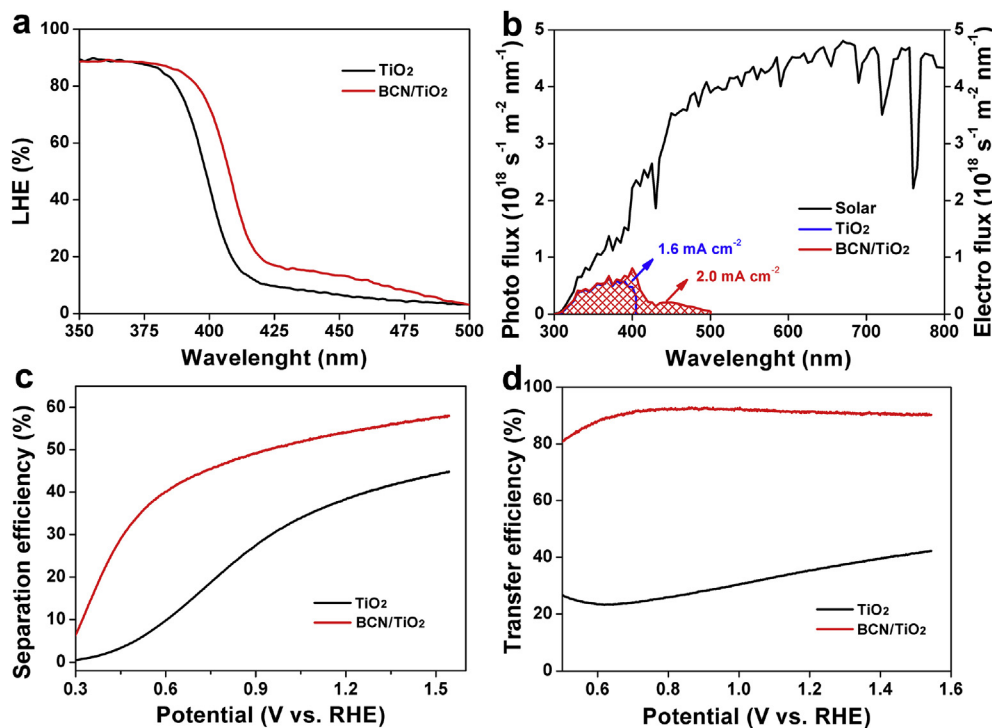


Fig. 6. Light harvesting efficiency (LHE) plots (a) and the AM 1.5 G photon flux incident at each wavelength and J_{abs} (b) of TiO₂ and BCN/TiO₂. The charge separation efficiency η_{sep} (c) and charge transfer efficiency $\eta_{transfer}$ (d) of TiO₂ and BCN/TiO₂.

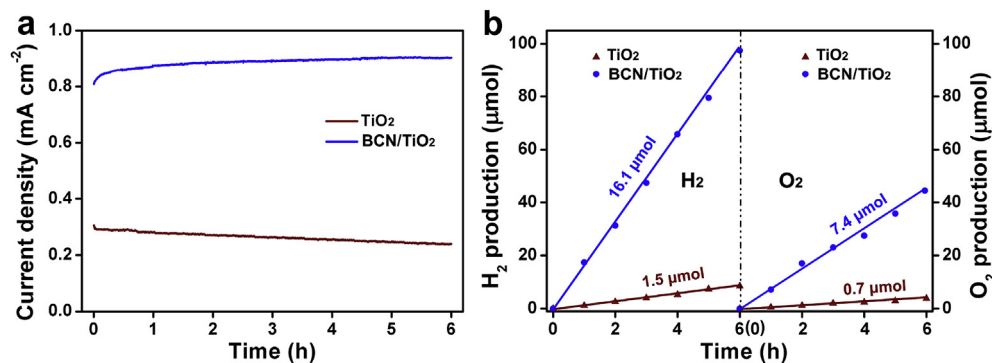


Fig. 7. (a) *i*-*t* curves of TiO₂ and BCN/TiO₂ photoanodes at 1.23 V vs. RHE. (b) Typical time course of H₂ and O₂ production from water for TiO₂ and BCN/TiO₂ under light illumination (100 mW cm⁻², AM 1.5 G), in which the dots represent experimental data and the solid lines are the fitting curves.

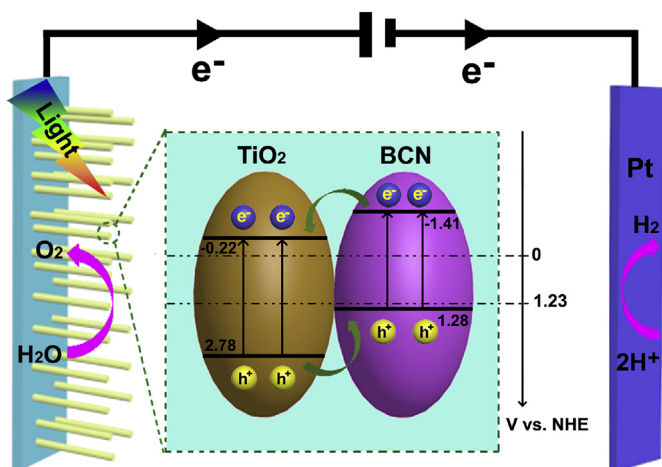


Fig. 8. Schematic illustration of the BCN/TiO₂ photoanode.

of BCN is calculated to be 5.72 eV by subtracting the secondary electron onset position of the He I UPS spectra from the excitation energy (21.2 eV) (Fig. S8) [51]. The valence band of TiO₂ is 7.22 eV as reported by our previous study [52]. The bandgap of TiO₂ and BCN are determined to be 3.0 eV and 2.69 eV from Tauc plots (Inset of Fig. 4b). Therefore, the conduction band (CB) of the TiO₂ and BCN is calculated to be 4.22 eV and 3.03 eV, respectively. According to the reference standard for which 0 V versus RHE equals -4.44 eV versus *evac* (vacuum level), the VB and CB values of TiO₂ and BCN in electron volts can be converted to electrochemical energy potentials in volts. Consequently, the VB values of TiO₂ and BCN are 2.78 and 1.28 V (vs. RHE), respectively. Obviously, the CB values for TiO₂ and BCN are -0.22 and -1.41 V (vs. RHE). Based on the matching band gap positions, a heterojunction is formed between the BCN and TiO₂, which is the driving force of charge transfer [53]. Under light illumination, BCN and TiO₂ absorb incident light and generate the electron-hole pairs. Attributed to the appropriate position and the built-in electric field, the photo-generated holes can transfer from TiO₂ to BCN, and electrons transfer in the opposite direction. Finally, the holes captured water molecular for O₂ evolution in the interface of photoanode/electrolyte, and the electrons are consumed by H⁺ for H₂ generation at the Pt counter electrode. Consequently, the BCN/TiO₂ increases the PEC water splitting.

4. Conclusions

In summary, the BCN/TiO₂ photoanode was successfully

synthesized by a facile thermal polymerization method. As results, the BCN/TiO₂ displays 4-fold increase of the photocurrent density (1.01 mA cm⁻²) at 1.23 V vs. RHE under irradiation (AM 1.5 G, 100 mW cm⁻²). And the onset potential of BCN/TiO₂ exhibits a negative shift with 100 mV. Attributed to the heterojunction between BCN and TiO₂, the charge separation and transfer efficiencies of the BCN/TiO₂ display a remarkable enhancement, which are 1.4 and 2.5 times (1.23 V vs. RHE) than that of TiO₂ photoanode, respectively. The maximum IPCE value is increased to 87.8% in 380 nm. Besides, the IPCE value approximately two times higher than that of TiO₂ in the entire visible region investigated. The constant H₂ evolution of BCN/TiO₂ is approximately 16.1 μmol h⁻¹ cm⁻² at 1.23 V (vs. RHE). The observation of this study provides rational strategies for designing composite photoelectrodes by tuning compositions and forming heterojunction to enhance PEC water splitting efficiency.

Acknowledgements

This work is supported by the National Natural Science Foundation of China (51602120, 51702114), Natural Science Foundation of Education Department of Henan Province (17A430023, 18A150011).

Appendix A. Supplementary data

Supplementary data related to this article can be found at <https://doi.org/10.1016/j.electacta.2018.06.090>.

References

- [1] M. Walter, E. Warren, J. McKone, S. Boettcher, Q. Mi, E. Santori, N. Lewis, Solar water splitting cells, *Chem. Rev.* 110 (2010) 6446–6473.
- [2] C. Jiang, S. Moniz, A. Wang, T. Zhang, J. Tang, Photoelectrochemical devices for solar water splitting-materials and challenges, *Chem. Soc. Rev.* 46 (2017) 4645–4660.
- [3] A. Fujishima, K. Honda, Electrochemical photolysis of water at a semiconductor electrode, *Nature* 237 (1972) 37–38.
- [4] P. Yilmaz, A. Lacerda, L. Larrosa, S. Dunn, Photoelectrocatalysis of rhodamine B and solar hydrogen production by TiO₂ and Pd/TiO₂ catalyst systems, *Electrochim. Acta* 231 (2017) 641–649.
- [5] H. Dotan, K. Sivula, M. Gratzel, A. Rothschild, S. Warren, Probing the photoelectrochemical properties of hematite (α-Fe₂O₃) electrodes using hydrogen peroxide as a hole scavenger, *Energy Environ. Sci.* 4 (2011) 958–964.
- [6] X. Chen, S. Shen, L. Guo, S. Mao, Semiconductor-based photocatalytic hydrogen generation, *Chem. Rev.* 110 (2010) 6503–6570.
- [7] E. Hendry, M. Koeberg, B. O'Regan, M. Bonn, Local field effects on electron transport in nanostructured TiO₂ revealed by terahertz spectroscopy, *Nano Lett.* 6 (2006) 755–759.
- [8] Y. Nah, I. Paramasivam, P. Schmuki, Doped TiO₂ and TiO₂ nanotubes: synthesis and applications, *ChemPhysChem* 11 (2010) 2698–2713.
- [9] Y. Tang, P. Wee, Y. Lai, X. Wang, D. Gong, P. Kanhere, T. Lim, Z. Dong, Z. Chen, Hierarchical TiO₂ nanoflakes and nanoparticles hybrid structure for improved

- photocatalytic activity, *J. Phys. Chem. C* 116 (2012) 2772–2780.
- [10] B. Aragaw, C. Pan, W. Su, H. Chen, J. Rick, B. Hwang, Facile one-pot controlled synthesis of Sn and C codoped single crystal TiO₂ nanowire arrays for highly efficient photoelectrochemical water splitting, *Appl. Catal., B* 163 (2015) 478–486.
 - [11] T. Fröschl, U. Hörmann, P. Kubiak, G. Kučerová, M. Pfanzt, C.K. Weiss, R.J. Behm, N. Hüsing, U. Kaiser, K. Landfester, M. Wohlfahrt-Mehrens, High surface area crystalline titanium dioxide: potential and limits in electrochemical energy storage and catalysis, *Chem. Soc. Rev.* 41 (2012) 5313–5360.
 - [12] X. Zhang, B. Zhang, Z. Zuo, M. Wang, Y. Shen, N/Si co-doped oriented single crystalline rutile TiO₂ nanorods for photoelectrochemical water splitting, *J. Mater. Chem. A* 3 (2015) 10020–10025.
 - [13] N. Lu, X. Quan, J. Li, S. Chen, H. Yu, G. Chen, Fabrication of boron-doped TiO₂ nanotube array electrode and investigation of its photoelectrochemical capability, *J. Phys. Chem. C* 111 (2007) 11836–11842.
 - [14] G. Bessegato, J. Cardoso, M. Zanon, Enhanced photoelectrocatalytic degradation of an acid dye with boron-doped TiO₂ nanotube anodes, *Catal. Today* 240 (2015) 100–106.
 - [15] X. Zhang, Y. Liu, S. Lee, S. Yang, Z. Kang, Coupling surface plasmon resonance of gold nanoparticles with slow-photon-effect of TiO₂ photonic crystals for synergistically enhanced photoelectrochemical water splitting, *Energy Environ. Sci.* 7 (2014) 1409–1419.
 - [16] T. Tatsuma, S. Saitoh, Y. Ohko, A. Fujishima, TiO₂-WO₃ Photoelectrochemical anticorrosion system with an energy storage ability, *Chem. Mater.* 13 (2001) 2838–2842.
 - [17] Z. Jiang, D. Jiang, Z. Yan, D. Liu, K. Qian, J. Xie, A new visible light active multifunctional ternary composite based on TiO₂-In₂O₃ nanocrystals heterojunction decorated porous graphitic carbon nitride for photocatalytic treatment of hazardous pollutant and H₂ evolution, *Appl. Catal., B* 170 (2015) 195–205.
 - [18] S. Moghiminia, H. Farsi, H. Raissi, Comparative optical and electrochemical studies of nanostructured NiTiO₃ and NiTiO₃-TiO₂ prepared by a low temperature modified sol-gel route, *Electrochim. Acta* 132 (2014) 512–523.
 - [19] F. Ning, M. Shao, S. Xu, Y. Fu, R. Zhang, M. Wei, D. Evans, X. Duan, TiO₂/graphene/NiFe-layered double hydroxide nanorod array photoanodes for efficient photoelectrochemical water splitting, *Energy Environ. Sci.* 9 (2016) 2633–2643.
 - [20] J. Liu, Y. Liu, N. Liu, Y. Han, X. Zhang, H. Huang, Y. Lifshitz, S. Lee, J. Zhong, Z. Kang, Metal-free efficient photocatalyst for stable visible water splitting via a two-electron pathway, *Science* 347 (2015) 970–974.
 - [21] X. Wang, K. Maeda, A. Thomas, K. Takanabe, G. Xin, J. Carlsson, K. Domen, M. Antonietti, A metal-free polymeric photocatalyst for hydrogen production from water under visible light, *Nat. Mater.* 8 (2009) 76–80.
 - [22] Y. Li, R. Wang, H. Li, X. Wei, J. Feng, K. Liu, Y. Dang, A. Zhou, Efficient and stable photoelectrochemical seawater splitting with TiO₂@g-C₃N₄ nanorod arrays decorated by Co-Pi, *J. Phys. Chem. C* 115 (2015) 20283–20292.
 - [23] T. Giannakopoulou, I. Papailias, N. Todorova, N. Boukos, Y. Liu, J. Yu, C. Trapalis, Tailoring the energy band gap and edges' potentials of g-C₃N₄/TiO₂ composite photocatalysts for NO_x removal, *Chem. Eng. J.* 310 (2017) 571–580.
 - [24] J. Wang, W. Zhang, Modification of TiO₂ nanorod arrays by graphite-like C₃N₄ with high visible light photoelectrochemical activity, *Electrochim. Acta* 71 (2012) 10–16.
 - [25] Y. Bu, Z. Chen, Effect of oxygen-doped C₃N₄ on the separation capability of the photoinduced electron-hole pairs generated by O-C₃N₄@TiO₂ with quasi-shell-core nanostructure, *Electrochim. Acta* 144 (2014) 42–49.
 - [26] C. Pan, J. Xu, Y. Wang, D. Li, Y. Zhu, Dramatic activity of C₃N₄/BiPO₄ photocatalyst with core/shell structure formed by self-assembly, *Adv. Funct. Mater.* 22 (2012) 1518–1524.
 - [27] W. Ma, D. Han, M. Zhou, H. Sun, L. Wang, X. Dong, L. Niu, Ultrathin g-C₃N₄/TiO₂ composites as photoelectrochemical elements for the real-time evaluation of global antioxidant capacity, *Chem. Sci.* 5 (2014) 3946–3951.
 - [28] S. Guo, Z. Deng, M. Li, B. Jiang, C. Tian, Q. Pan, H. Fu, Phosphorus-doped carbon nitride tubes with a layered micro-nanostructure for enhanced visible-light photocatalytic hydrogen evolution, *Angew. Chem. Int. Ed.* 55 (2016) 1830–1834.
 - [29] J. Su, P. Geng, X. Li, Q. Zhao, X. Quan, G. Chen, Novel phosphorus doped carbon nitride modified TiO₂ nanotube arrays with improved photoelectrochemical performance, *Nanoscale* 7 (2015) 16282–16289.
 - [30] S. Lin, X. Ye, X. Gao, J. Huang, Mechanistic insight into the water photooxidation on pure and sulfur-doped g-C₃N₄ photocatalysts from DFT calculations with dispersion corrections, *J. Mol. Catal. Chem.* 406 (2015) 137–144.
 - [31] G. Zhang, M. Zhang, X. Ye, X. Qiu, S. Lin, X. Wang, Iodine modified carbon nitride semiconductors as visible light photocatalysts for hydrogen evolution, *Adv. Mater.* 26 (2014) 805–809.
 - [32] Y. Yan, Z. Li, Z. Zou, Photodegradation of rhodamine B and methyl orange over boron-doped g-C₃N₄ under visible light irradiation, *Langmuir* 26 (2010) 3894–3901.
 - [33] Q. Ruan, W. Luo, J. Xie, Y. Wang, X. Liu, Z. Bai, C. Carmalt, J. Tang, A nanojunction polymer photoelectrode for efficient charge transport and separation, *Angew. Chem. Int. Ed.* 56 (2017) 8221–8225.
 - [34] G. Govindaraju, G. Wheeler, D. Lee, K. Choi, Methods for electrochemical synthesis and photoelectrochemical characterization for photoelectrodes, *Chem. Mater.* 29 (2017) 355–370.
 - [35] S. Zhao, J. Liu, C. Li, W. Ji, M. Yang, H. Huang, Y. Liu, Z. Kang, Tunable ternary (N, P, B)-doped porous nanocarbons and their catalytic properties for oxygen reduction reaction, *ACS Appl. Mater. Interfaces* 6 (2014) 22297–22304.
 - [36] F. Boccuzzi, A. Chiorino, M. Manzoli, D. Andreeva, T. Tabakova, FT-IR study of the low-temperature water-gas shift reaction on Au/Fe₂O₃ and Au/TiO₂ catalysts, *J. Catal.* 188 (1999) 176–185.
 - [37] M. Kawaguchi, T. Kawashima, T. Nakajima, Syntheses and structures of new graphite-like materials of composition BCN(H) and BC₃N(H), *Chem. Mater.* 8 (1996) 1197–1201.
 - [38] L. Song, L. Ci, H. Lu, P. Sorokin, C. Jin, J. Ni, A. Kvashnin, D. Kvashnin, J. Lou, B. Yakobson, P. Ajayan, Large scale growth and characterization of atomic hexagonal boron nitride layers, *Nano Lett.* 10 (2010) 3209–3215.
 - [39] X. Pan, M. Yang, X. Fu, Z. Zhang, X. Xu, Defective TiO₂ with oxygen vacancies: synthesis, properties and photocatalytic applications, *Nanoscale* 5 (2013) 3601–3614.
 - [40] Y. Wang, Y. Shao, D. Matson, J. Li, Y. Lin, Nitrogen-doped graphene and its application in electrochemical biosensing, *ACS Nano* 4 (2010) 1790–1798.
 - [41] E. Hosono, S. Fujihara, H. Imai, I. Honma, I. Masaki, H. Zhou, One-step synthesis of nano-micro chestnut TiO₂ with rutile nanopins on the microanatase octahedron, *ACS Nano* 1 (2007) 273–278.
 - [42] I. Cho, Z. Chen, A. Forman, D. Kimm, P. Rao, T. Jaramillo, X. Zhen, Branched TiO₂ nanorods for photoelectrochemical hydrogen production, *Nano Lett.* 11 (2011) 4978–4984.
 - [43] G. Li, E. Sproviero, W. McNamara, R. Snoeberger, R. Crabtree, G. Brudvig, V. Batista, Reversible visible-light photooxidation of an oxomanganese water-oxidation catalyst covalently anchored to TiO₂ nanoparticles, *J. Phys. Chem. B* 114 (2010) 14214–14222.
 - [44] K. Schwinghammer, M. Mesch, V. Duppel, C. Ziegler, J. Senker, B. Lotsch, Crystalline carbon nitride nanosheets for improved visible-light hydrogen evolution, *J. Am. Chem. Soc.* 136 (2014) 1730–1733.
 - [45] J. Gunjekar, T. Kim, H. Kim, I. Kim, S. Hwang, Mesoporous layer-by-layer ordered nanohybrids of layered double hydroxide and layered metal oxide: highly active visible light photocatalysts with improved chemical stability, *J. Am. Chem. Soc.* 133 (2011) 14998–15007.
 - [46] D. Zhang, C. Pang, X. Wang, The function-led design of Z-scheme photocatalytic systems based on hollow carbon nitride semiconductors, *Chem. Commun.* 51 (2015) 17467–17470.
 - [47] Q. Yu, X. Meng, T. Wang, P. Li, J. Ye, Hematite films decorated with nanostructured ferric oxyhydroxide as photoanodes for efficient and stable photoelectrochemical water splitting, *Adv. Funct. Mater.* 25 (2015) 2686–2692.
 - [48] F. Abdi, L. Han, A. Smets, M. Zeman, B. Dam, R. Krol, Efficient solar water splitting by enhanced charge separation in a bismuth vanadate-silicon tandem photoelectrode, *Nat. Commun.* 4 (2013) 2195.
 - [49] J. Seabold, K. Choi, Efficient and stable photo-oxidation of water by a bismuth vanadate photoanode coupled with an iron oxyhydroxide oxygen evolution catalyst, *J. Am. Chem. Soc.* 134 (2012) 2186–2192.
 - [50] T. Kim, K. Choi, Nanoporous BiVO₄ photoanodes with dual-layer oxygen evolution catalysts for solar water splitting, *Science* 343 (2014) 990–994.
 - [51] G. Liu, W. Jaegermann, J. He, V. Sundström, L. Sun, XPS and UPS Characterization of the TiO₂/ZnPCl₂ heterointerface: alignment of energy levels, *J. Phys. Chem. B* 106 (2002) 5814–5819.
 - [52] X. Zhang, B. Zhang, K. Cao, J. Brillet, J. Chen, M. Wang, S. Yan, A perovskite solar cell-TiO₂/BiVO₄ photoelectrochemical system for direct solar water splitting, *J. Mater. Chem. A* 3 (2015) 21630–21636.
 - [53] M. Gui, W. Zhang, Q. Su, C. Chen, Preparation and visible light photocatalytic activity of Bi₂O₃/Bi₂WO₆ heterojunction photocatalysts, *J. Solid State Chem.* 184 (2011) 1977–1982.